



PAPER

RECEIVED
15 February 2018REVISED
25 April 2018ACCEPTED FOR PUBLICATION
1 May 2018PUBLISHED
22 May 2018

Y-90 SPECT ML image reconstruction with a new model for tissue-dependent bremsstrahlung production using CT information: a proof-of-concept study

Hongki Lim¹, Jeffrey A Fessler¹, Scott J Wilderman³, Allen F Brooks² and Yuni K Dewaraja²¹ Department of Electrical Engineering and Computer Science, University of Michigan, Ann Arbor, MI 48109, United States of America² Department of Radiology, University of Michigan, Ann Arbor, MI 48109, United States of America³ Department of Nuclear Engineering and Radiological Sciences, University of Michigan, Ann Arbor, MI 48109, United States of AmericaE-mail: hongki@umich.edu, fessler@umich.edu, sjwnc@umich.edu, afb@umich.edu and yuni@med.umich.edu**Keywords:** bremsstrahlung, SPECT, SPECT/CT, Yttrium-90, Y-90, quantification, reconstruction

Abstract

While the yield of positrons used in Y-90 PET is independent of tissue media, Y-90 SPECT imaging is complicated by the tissue dependence of bremsstrahlung photon generation. The probability of bremsstrahlung production is proportional to the square of the atomic number of the medium. Hence, the same amount of activity in different tissue regions of the body will produce different numbers of bremsstrahlung photons. Existing reconstruction methods disregard this tissue-dependency, potentially impacting both qualitative and quantitative imaging of heterogeneous regions of the body such as bone with marrow cavities. In this proof-of-concept study, we propose a new maximum-likelihood method that incorporates bremsstrahlung generation probabilities into the system matrix, enabling images of the desired Y-90 distribution to be reconstructed instead of the ‘bremsstrahlung distribution’ that is obtained with existing methods. The tissue-dependent probabilities are generated by Monte Carlo simulation while bone volume fractions for each SPECT voxel are obtained from co-registered CT. First, we demonstrate the tissue dependency in a SPECT/CT imaging experiment with Y-90 in bone equivalent solution and water. Visually, the proposed reconstruction approach better matched the true image and the Y-90 PET image than the standard bremsstrahlung reconstruction approach. An XCAT phantom simulation including bone and marrow regions also demonstrated better agreement with the true image using the proposed reconstruction method. Quantitatively, compared with the standard reconstruction, the new method improved estimation of the liquid bone:water activity concentration ratio by 40% in the SPECT measurement and the cortical bone:marrow activity concentration ratio by 58% in the XCAT simulation.

1. Introduction

Novel therapeutic applications have sparked growing interest in quantitative imaging of Y-90, an almost pure beta emitter (average energy, 0.94 MeV; mean tissue penetration, 2.5 mm; half-life, 64 h) that is used in internal radionuclide therapy. Applications where Y-90 imaging has been used include microsphere radioembolization of hepatic malignancies (Smits *et al* 2015), peptide receptor radionuclide therapy of neuroendocrine tumors (Fabbri *et al* 2012) and ibritumomab radioimmunotherapy (Minarik *et al* 2010) of non-Hodgkins lymphoma. Additionally, Y-90 imaging has been reported in radiation synovectomy, a treatment option for inflammation of the synovium membrane found in joints such as the knee (Barber *et al* 2013). In such therapies, the lack of gamma photons simplifies radioprotection of surrounding organs and personnel, but it makes imaging of Y-90 complex; it involves SPECT via bremsstrahlung photons associated with the Y-90 betas or PET via a very low abundance positron associated with Y-90 decay (Minarik *et al* 2008, Van Elmbt *et al* 2011). PET has the advantage of superior resolution over bremsstrahlung SPECT, but a disadvantage is the high noise associated with low

(true) count-rates in the presence of high randoms (Smits *et al* 2015). For this reason, and because of the wider accessibility of SPECT, interest in bremsstrahlung imaging of Y-90 continues.

While the yield of positrons used in Y-90 PET is independent of the tissue media, the yield of bremsstrahlung photons used in SPECT is tissue dependent. The Y-90 bremsstrahlung yield consists of 2 components: internal bremsstrahlung (IB) and external bremsstrahlung (EB) (Venkataramaiah *et al* 1980, Cengiz and Almaz 2004, Walrand *et al* 2018). The bremsstrahlung energy spectra corresponding to both components extend from zero to the beta endpoint energy, 2.3 MeV for Y-90. IB arises during the beta decay process itself, while EB photons are produced as beta particles pass through the media containing the radioisotope and are accelerated in the Coulomb fields of atomic nuclei and electrons of the medium. The IB energy spectrum is thus a property of the emitter, while the EB energy spectrum depends on both the energy spectrum of the beta emitter and the material properties of the surrounding medium. Most significantly, the cross section describing the production of EB, based on the Bethe–Heitler formula (Bethe and Heitler 1934), is proportional to Z^2 where Z is the atomic number of the tissue medium.

As a consequence of the Z^2 dependence of the EB production probability, the same amount of Y-90 activity in different tissue regions of the body will generate significantly different numbers of bremsstrahlung photons, which impacts both qualitative and quantitative assessment of Y-90 SPECT images. The difference in bremsstrahlung production probabilities (per beta decay) is particularly significant when comparing bone and soft tissue.

Although specialized reconstruction methods have been developed for Y-90 SPECT imaging (Rong *et al* 2012, Elschot *et al* 2013, Dewaraja *et al* 2017), these methods have not accounted for the tissue-dependent bremsstrahlung yield. This paper reports simulations and experimental measurements to demonstrate the effect and implement and test a reconstruction formulation that accounts for the tissue dependency of bremsstrahlung generation in the SPECT system model. The method relies on co-registered CT to determine the tissue composition of each SPECT voxel, which is facilitated by the availability of hybrid SPECT-CT.

2. Methods

2.1. Image reconstruction with a tissue dependent system model

Maximum likelihood (ML) image reconstruction performs the following optimization with respect to an image \mathbf{x} :

$$\hat{\mathbf{x}} = \underset{\mathbf{x} \geq 0}{\operatorname{argmin}} f(\mathbf{x}), \quad f(\mathbf{x}) = \sum_{i=1}^{n_d} \bar{y}_i(\mathbf{x}) - y_i \log \bar{y}_i(\mathbf{x}), \quad (1)$$

where n_d is the number of rays, $f(\mathbf{x})$ is the Poisson negative log-likelihood between measurement \mathbf{y} and estimated measurement means $\bar{\mathbf{y}}(\mathbf{x})$, and $\bar{\mathbf{y}}(\mathbf{x}) = \mathbf{A}\mathbf{x} + \bar{\mathbf{r}}$. The matrix \mathbf{A} denotes the system model, incorporating factors such as attenuation coefficients. $\bar{\mathbf{r}}$ denotes the mean background events such as scatter and random coincidence.

We incorporate the tissue-dependent probability into the image reconstruction by multiplying the system matrix \mathbf{A} by a matrix \mathbf{B} that models the bremsstrahlung spectra produced in each voxel as a bone volume fraction (BVF) weighted mixture of the bone-only and tissue-only spectra. We consider only two media, bone and soft-tissue where the bremsstrahlung generation probability differs highly, but the method can be easily extended to include more media. The new system model $\tilde{\mathbf{A}}$ can be expressed as:

$$\tilde{\mathbf{A}} = \mathbf{A}\mathbf{B} = \begin{bmatrix} a_{11} & a_{12} & \dots & a_{1n_p} \\ a_{21} & a_{22} & \dots & a_{2n_p} \\ a_{31} & a_{32} & \dots & a_{3n_p} \\ \dots & \dots & \dots & \dots \\ a_{n_d1} & a_{n_d2} & \dots & a_{n_dn_p} \end{bmatrix} \begin{bmatrix} b_1 & 0 & \dots & 0 \\ 0 & b_2 & \dots & 0 \\ \dots & \dots & \dots & 0 \\ 0 & 0 & \dots & b_{n_p} \end{bmatrix}, \quad (2)$$

where n_p is the number of voxels of the unknown image \mathbf{x} and \mathbf{B} is a diagonal matrix with diagonal elements:

$$b_j = 1 - \text{BVF}_j + q_{\text{bone}} \cdot \text{BVF}_j. \quad (3)$$

q_{bone} is the bremsstrahlung photon generation probability ratio between bone and tissue. BVF_j is a BVF of j th voxel in SPECT and we use CT information (attenuation coefficients) to determine the BVF of each voxel in SPECT:

$$\text{BVF} = g(\boldsymbol{\eta}) \quad (4)$$

$$\eta_k = \begin{cases} 1, & \mu_k \geq c \\ 0, & \mu_k < c, \end{cases} \quad (5)$$

where η is a mask image indicating bone voxels and g denotes an interpolating function to relate CT sized mask image with SPECT sized BVF image. μ_k is the k th voxel of the attenuation map and a constant c is the threshold value to determine if a voxel is bone or tissue. We set c value as 80% of the maximum value of the attenuation map.

2.2. Bremsstrahlung yield in different tissue

To obtain the tissue dependent (external) bremsstrahlung probabilities to include in the above system model, we performed simulations using the *pencil* program of the PENELOPE (version 2014) Monte Carlo electron/photon transport package (Salvat *et al* 2006). The PENELOPE database of bremsstrahlung differential cross sections are based on the partial-wave database compiled by Seltzer and Berger (1986). For the present simulations, the Y-90 beta emission spectrum from the *BetaShape* program (Mougeot 2015) was coupled with PENELOPE. The PENELOPE database of pre-defined materials, which is adapted from the database of the ESTAR program of Berger (1992), was used for media definition. The cutoff energy for particle transport termination with remaining energy assumed to be locally absorbed was set at 10 keV for both electrons and photons. PENELOPE generated EB emission spectra by simulating a Y-90 point source in an infinite geometry for the medium of interest: ICRP cortical bone, marrow, tissue and lung tissue. Additionally, for comparison with bone, we generated the EB spectrum for Y-90 in K_2HPO_4 solution to justify the choice of this salt as a bone equivalent medium in the experiment described below. We constructed the bremsstrahlung energy spectrum by tallying the emitted photon energy at the point of generation, before any potential self-absorption. The Y-90 IB spectrum, based on the Knipp, Uhlenbeck and Bloch (KUB) theory was taken from the work of Cengiz and Almaz (2004). We combined the PENELOPE-generated EB spectra (in absolute units of photons/eV/decay) with the theoretical absolute IB spectrum to produce total Y-90 bremsstrahlung emission spectra for the different media.

2.3. Experimental measurement and phantom simulation

To demonstrate the impact of tissue dependent bremsstrahlung generation on SPECT imaging and to evaluate the performance of bremsstrahlung SPECT reconstruction with the above tissue dependent system model, we performed an experimental measurement and a phantom simulation study with Y-90 in bone and tissue media.

2.3.1. SPECT/CT measurement with Y-90 in tissue and bone equivalent media

The experiment was performed with Y-90 in tissue-equivalent (water) and bone equivalent material. The bone equivalent liquid solution was prepared by dissolving K_2HPO_4 salt (dipotassium hydrogen phosphate) in DI water to form a saturated solution of K_2HPO_4 . Anhydrous K_2HPO_4 (298.5 g) was dissolved in 200 ml of DI water by use of magnetic stirring with the mixture covered until solution was achieved (1 h). This solution mimics density and effective Z number of cranium bone (de Dreuille *et al* 1997). A chelator (2.5 μ M EDTA; appropriate amount from a 1 M EDTA diammonium salt hydrate stock solution) was added to the solution to avoid adherence of Y-90 to plastic walls (Park *et al* 2008). 40 ml of the bone equivalent solution was mixed with 25 MBq of Y-90 in a 60 ml plastic syringe. A second syringe with water (to mimic tissue) was prepared with the same geometry and Y-90 concentration as in the bone-equivalent syringe.

The bone and tissue equivalent syringes were positioned as shown in figure 1(a) and imaged with a Siemens Intevo SPECT/CT system equipped with a high energy general purpose collimator. A 105–195 keV bremsstrahlung acquisition window was selected based on our previous work (Dewaraja *et al* 2017). The following acquisition parameters were used: 180° and 64 views per head with 15 s/view; step-and-shoot; a 128 × 128 matrix with a pixel size of 4.8 mm. The CT component of acquisition used full circle rotation, 130 kV, 80 mAs and was reconstructed with a 512 × 512 × 196 matrix (0.98 mm × 0.98 mm × 2 mm voxel size).

The CT-based attenuation map (at 150 keV, the center energy of the acquisition window) generated with the camera software was saved for attenuation correction and to determine the voxel-level BVFs for the new system model of section 2.1. At 150 keV bremsstrahlung generation probability in bone equivalent liquid is 1.4 times the probability in water according to the simulation results discussed in section 3.1. Therefore q_{bone} in (6) was also set as 1.4 for reconstructing images with the proposed model. We reconstructed images with in-house 3D OS-EM (Koral *et al* 2007) including attenuation, collimator detector response and without and with tissue-dependent probabilities (with and without matrix \mathbf{B} in (2)). The reconstruction parameters (15 iterations 8 subsets and no post-smoothing) were chosen based on previous phantom studies (Dewaraja *et al* 2017). In addition, for comparison we also reconstructed images using Siemens Flash3D OS-EM software, including attenuation correction and collimator detector response.

Additionally, for comparison, Y-90 PET/CT was also performed for the same source geometry. Data was acquired with a Siemens Biograph mCT scanner and was reconstructed with Siemens 3D-OS-EM software including point-spread function and time-of-flight information using 1 iteration, 21 subsets and a 5 mm FWHM Gaussian post-filter. The matrix size was 200 × 200 (pixel size 4.07 mm). These PET parameters were chosen based on a previous phantom study (Dewaraja *et al* 2015).

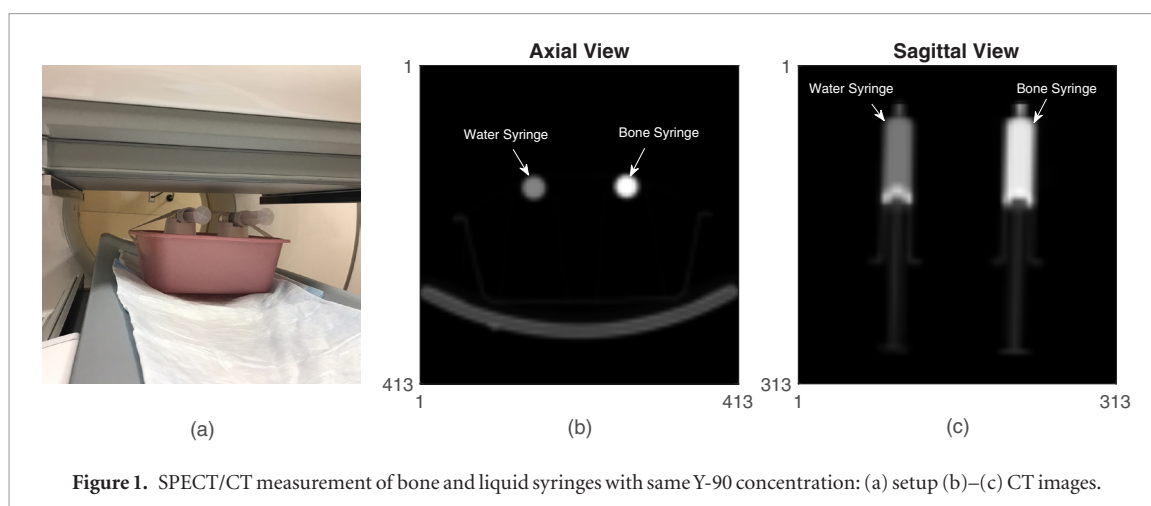


Figure 1. SPECT/CT measurement of bone and liquid syringes with same Y-90 concentration: (a) setup (b)–(c) CT images.

2.3.2. XCAT simulations

A clinically realistic geometry was simulated using the region from spine to upper femur of the XCAT phantom (Segars *et al* 2010). We considered a case where the true activity concentration ratio is 1:1 for bone:marrow. However, when generating the projection measurement \mathbf{y} in (1), we changed the value of voxels corresponding to ICRP bone to represent the 1.6 times higher bremsstrahlung photon generation probability in bone relative to marrow (at 150 keV bremsstrahlung generation probability in bone is 1.6 times the probability in marrow according to the PENELOPE results discussed in section 3.1). Figure 2(c) shows the activity map with different bremsstrahlung generation probability when the true activity map is figure 2(b). SPECT projection data for this digital phantom were generated using an analytical projector, which included non-uniform attenuation and the collimator detector response of the SPECT camera⁴. Images were reconstructed with in-house developed 3D OS-EM (35 iterations 8 subsets) including attenuation, collimator detector response and without and with tissue-dependent probabilities (q_{bone} in equation (3) set as 1.6).

3. Results

3.1. Bremsstrahlung yield in different tissue

Figure 3 and table 1 compare the total (external + internal) bremsstrahlung yield in the different media. While the yield in lung and different soft tissue media (soft tissue, red marrow and yellow marrow) are very similar, the yield in bone is substantially higher. In the energy range of the SPECT acquisition window (100–200 keV) bremsstrahlung production is 1.6–1.7 times as high in bone as in other tissue. Figure 4(a) compares the bremsstrahlung yield for the K_2HPO_4 solution versus cranium bone and for water versus soft-tissue to demonstrate equivalence of the media used in the experiment to true bone and tissue. Additionally, mass attenuation coefficients over a range of energies were generated by inputting the compositions to the XCOM database⁵ and the corresponding linear attenuation coefficients compared in figure 4(b) also demonstrate equivalence.

3.2. SPECT measurement with tissue and bone equivalent media

Figures 5(a)–(d) are the syringe images reconstructed using commercial PET and SPECT software. The PET image shows that the two syringes have similar Y-90 activity concentration (true concentrations are equal) because PET depends on positron emission, which is not tissue dependent. However, the SPECT image shows that the bone syringe has significantly higher concentration than the water syringe because of the higher bremsstrahlung yield in bone. Figure 6(a) is the profile at the center of the syringes (in relative units). The peaks of the profile corresponding to the two syringes in PET are identical whereas in SPECT the peak of the bone syringe is 1.4 times higher than that of the water syringe, which is attributed to the 1.4 times higher bremsstrahlung production probability in liquid bone compared with water in the energy range of the SPECT acquisition window (table 1).

Figures 5(e)–(h) are the SPECT images reconstructed using the Michigan image reconstruction toolbox (MIRT)⁶ without and with incorporating tissue-dependent probabilities into the system matrix. The image reconstructed with the new model shows that the two syringes have similar concentration of Y-90. Also, the peaks

⁴<http://web.eecs.umich.edu/~fessler/aspire/index.html>

⁵<https://physics.nist.gov/PhysRefData/Xcom/html/xcom1.html>

⁶https://gitlab.eecs.umich.edu/fessler/mirt_mat

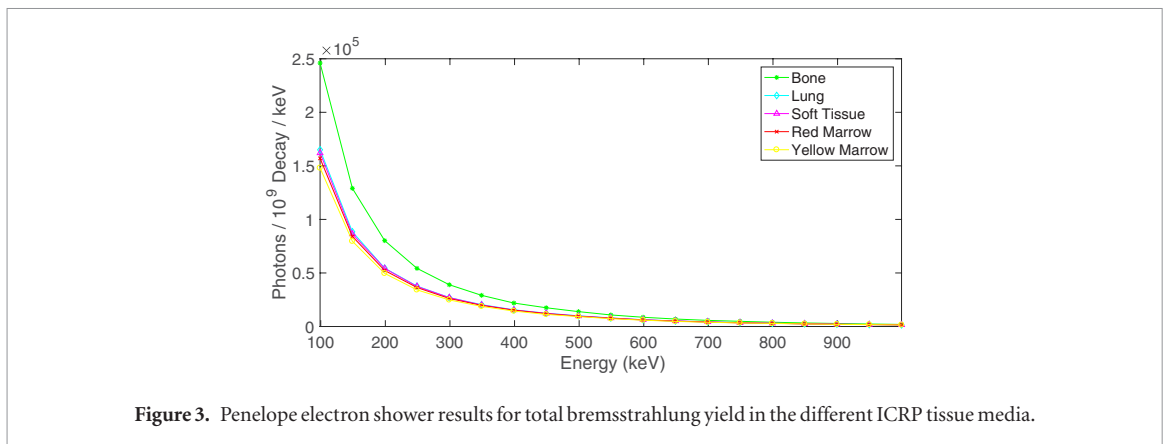
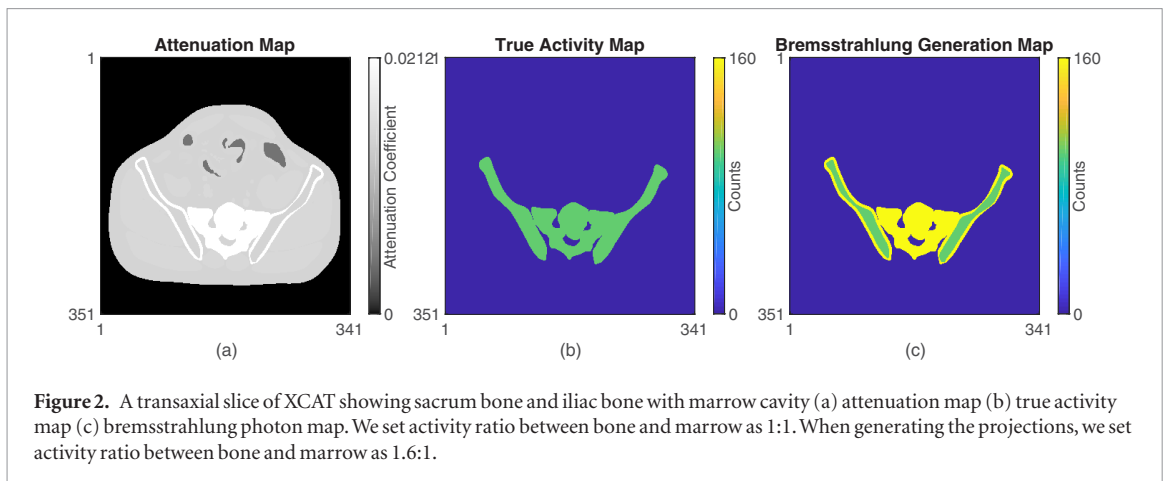
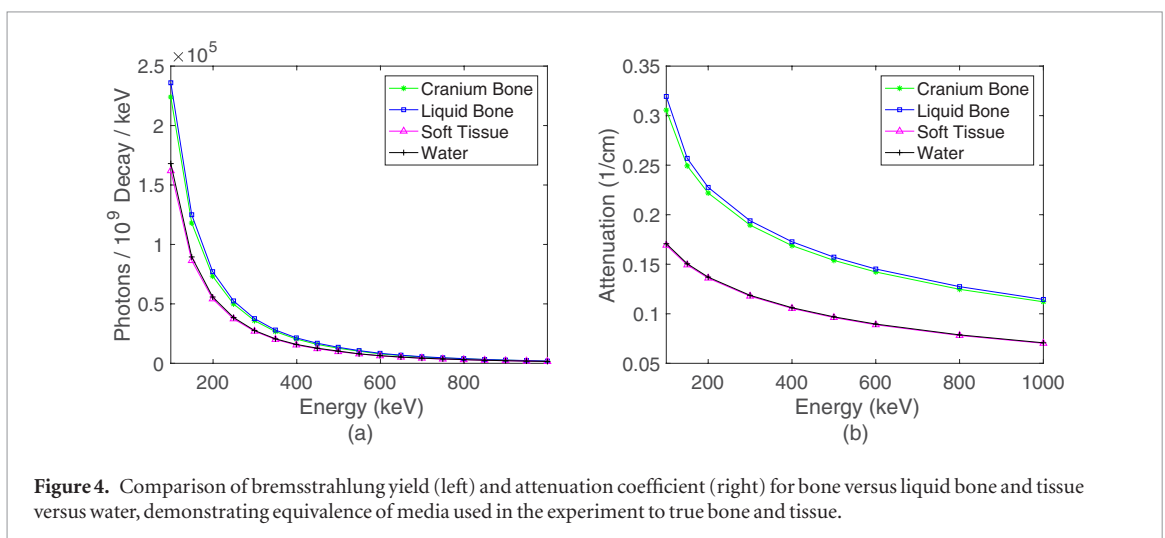
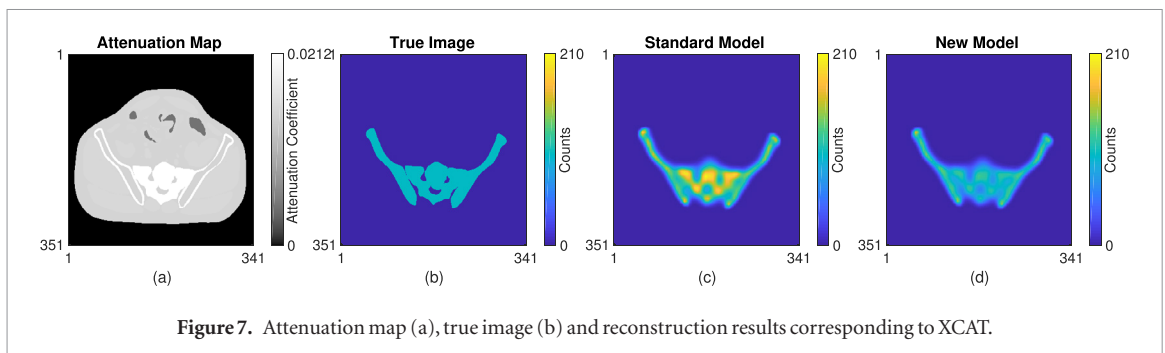
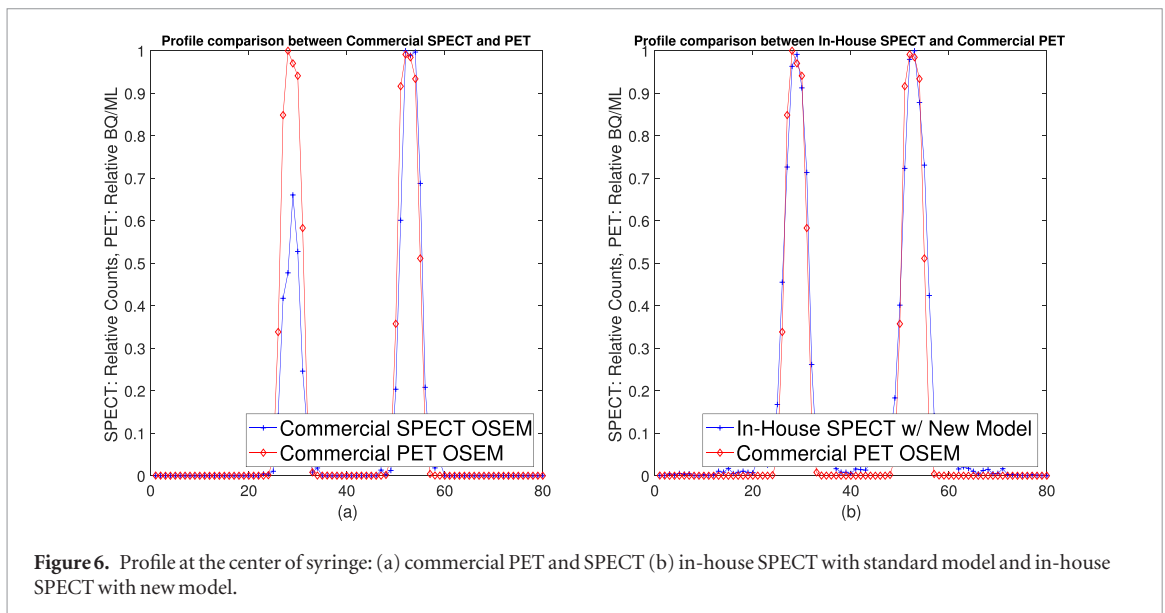
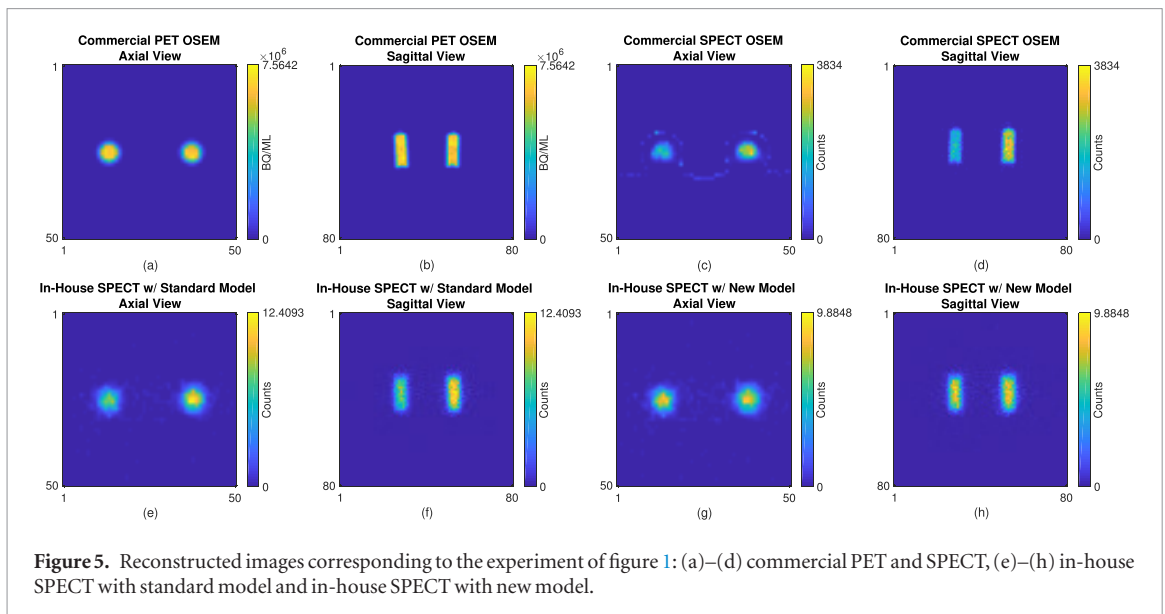


Table 1. Total bremsstrahlung yield in different media as a function of energy.

keV	Photons/keV/10 ⁹ decays					
	Bone	Marrow	Bone:Marrow ratio	Liquid bone	Water	Liquid bone:Water ratio
50	6.87×10^5	4.06×10^5	1.69	6.61×10^5	4.66×10^5	1.42
100	2.43×10^5	1.45×10^5	1.67	2.34×10^5	1.66×10^5	1.41
150	1.28×10^5	7.84×10^4	1.64	1.24×10^5	8.85×10^4	1.40
200	7.89×10^4	4.92×10^4	1.61	7.71×10^4	5.55×10^4	1.39
500	1.37×10^4	9.12×10^3	1.50	1.34×10^4	1.01×10^4	1.32
1000	2.01×10^3	1.48×10^3	1.35	1.92×10^3	1.55×10^3	1.24





of the profile corresponding to the two syringes become identical (as in the PET profile) when we incorporate the tissue-dependent probability as shown in figure 6(b).

For quantitative evaluation of SPECT images, we compared the liquid bone to water count concentration ratio in two syringes to the true activity concentration ratio (equal to 1.0). The new model gives a ratio of 1.03 while the standard model gives a ratio of 1.43 because of overestimating the counts in the bone syringe.

3.3. XCAT simulations

We compared SPECT reconstructions using the new model and standard model. For visualization and evaluation, we interpolated SPECT image to match the CT image size. Visually, there is substantially better

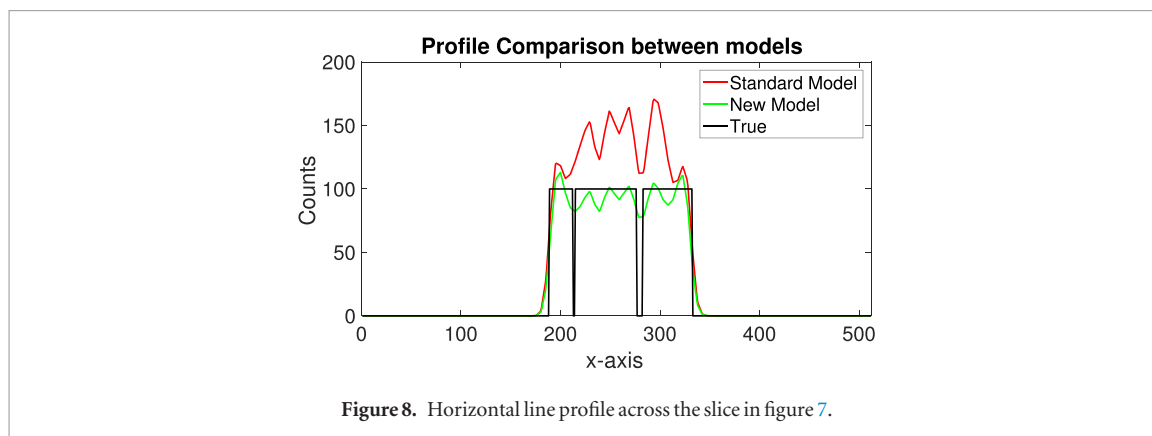


Table 2. EB and IB stand for external and IB, respectively. Comparison of including and excluding IB in liquid bone and water. Without modeling the IB, we would set q_{bone} as 1.6 rather than 1.4.

keV	Photons/keV/ 10^9 decays					
	Liquid bone (EB)	Water (EB)	Ratio	Liquid bone (IB+EB)	Water (IB+EB)	Ratio
50	5.62×10^5	3.67×10^5	1.53	6.61×10^5	4.66×10^5	1.42
100	1.90×10^5	1.22×10^5	1.56	2.34×10^5	1.66×10^5	1.41
150	9.66×10^4	6.15×10^4	1.57	1.24×10^5	8.85×10^4	1.40
200	5.84×10^4	3.69×10^4	1.59	7.71×10^4	5.55×10^4	1.39
500	8.37×10^3	5.13×10^3	1.63	1.34×10^4	1.01×10^4	1.32
1000	8.50×10^2	5.07×10^2	1.38	1.92×10^3	1.55×10^3	1.24

agreement between the SPECT reconstruction and the true activity map when the system model included the tissue dependent probability (figures 7 and 8).

As in the experiment, for a quantitative evaluation, we compared the bone to marrow count concentration ratio to the true activity concentration ratio (equal to 1.0). The new model gives a ratio of 1.06 while the standard model gives a ratio of 1.64 because of overestimating the counts in the bone region. Here, we used a small VOI (56 voxels per slice, 3 slices) at the center of the bone and marrow regions to exclude partial volume effects.

4. Discussion and conclusions

In this study we showed the impact of tissue-dependent bremsstrahlung generation on both qualitative and quantitative Y-90 SPECT/CT imaging and investigated a new reconstruction formalism to correct for this effect. The new reconstruction system model uses Monte Carlo (PENELOPE) derived bremsstrahlung generation probabilities and CT-derived bone volume fractions in each voxel. We used a potassium salt, which we showed is equivalent to cranium bone in terms of bremsstrahlung yield and attenuation coefficient, to experimentally demonstrate the tissue dependency. In the SPECT/CT measurement with equal concentrations of Y-90 in bone and tissue equivalent liquids, the count concentration in the bone region was significantly higher than in the tissue region with standard reconstruction, but approached the true distribution with the new reconstruction model. Similar improvements were also demonstrated for the XCAT phantom when activity in bone was ‘artificially’ increased relative to marrow to mimic the higher bremsstrahlung generation probability. For quantifying the activity concentration ratio in two media the new reconstruction performed 40% (the proposed method had 3% error whereas the standard method had 43% error) better than the standard reconstruction in the experimental study and 58% (the proposed method had 6% error whereas the standard method had 64% error) better than the standard reconstruction in the XCAT study. This improvement is made without additional heavy computational cost or memory consumption. With our computer (Intel Core i7-7700K), 35 iterations (with 8 subsets) of standard model required 16.4 s whereas proposed algorithm took 16.6 s.

Prior to the recent study of Walrand *et al* (2018) where the importance of IB was highlighted, Y-90 SPECT (simulation) studies ignored the contribution of IB. However, as we did in the current study, including this component, which is not Z dependent, is important for getting the exact value of q_{bone} . Table 2 shows how the yield ratio for the two media would be changed if we only included the Z-dependent EB component. For the experiment with liquid bone, we would set the q_{bone} as 1.6 rather than 1.4. based on this yield ratio. However, setting q_{bone} as 1.6 would result in the underestimation of counts in bone syringe ($1.03 \rightarrow 0.94$).

Dividing standard reconstruction by the matrix \mathbf{B} in (2) could be an alternative approach for incorporating the tissue dependent effects although this approach does not correctly model the statistical (Poisson) nature of the acquisition. We evaluated this post-reconstruction approach using the experiment data with bone and tissue equivalent syringes in figure 1. We found that this alternative method gives the same quantification result as our proposed method (liquid bone to water count concentration: 1.03). However, there was a difference between images generated by this approach and our proposed method (difference in voxel counts of the two image ranges from -4.1% – 4.0% of each voxel count). Moreover, it would lead to different result compared to our method when $f(\mathbf{x})$ in (1) includes the regularization term for penalizing the image roughness and controlling noise in extreme imaging cases (e.g. low-count setting) because the weight of likelihood term and that of regularization term for the updates can differ due to including/excluding \mathbf{B} . Additionally, the computation cost of the alternative approach is equivalent to our method, therefore there is no disadvantage to using our more accurate formulation.

SPECT-CT misalignment due to motion may reduce the benefits of the proposed method where CT information was used to determine voxel-level bone volume fractions. Evaluating the new method using XCAT simulations that include motion is potential future work. Moreover, this paper is a proof-of-concept study to demonstrate that the bremsstrahlung generation probabilities can be included in the reconstruction model to improve qualitative and quantitative Y-90 SPECT/CT imaging. However, further investigation of the impact on clinical studies is required. For large homogeneous organs such as the liver, the new model is likely not needed, however, our proposed method becomes important in heterogeneous regions with bone-tissue interfaces.

To conclude, Y-90 SPECT imaging of heterogeneous regions is significantly enhanced by including tissue-dependent bremsstrahlung generation probabilities in the SPECT system matrix without adding substantial computation cost.

Acknowledgment

This work was supported by grant R01 EB022075, awarded by the National Institute of Biomedical Imaging and Bioengineering, National Institute of Health, US Department of Health and Human Services.

ORCID iDs

Hongki Lim  <https://orcid.org/0000-0002-2764-3730>

Jeffrey A Fessler  <https://orcid.org/0000-0001-9998-3315>

Yuni K Dewaraja  <https://orcid.org/0000-0002-3920-6925>

References

- Barber T W, Yap K S, Cherk M H, Powell A and Kalff V 2013 Comparison of positron emission tomography/CT and bremsstrahlung imaging following Y-90 radiation synovectomy *J. Med. Imaging Radiat. Oncol.* **57** 567–71
- Berger M J 1992 ESTAR, PSTAR, and ASTAR: computer programs for calculating stopping-power and range tables for electrons, protons, and helium ions *Report NISTIR 4999* (Gaithersburg, MD: National Institute of Standards and Technology)
- Bethe H and Heitler W 1934 On the stopping of fast particles and on the creation of positive electrons *Proc. R. Soc. A* **146** 83–112
- Cengiz A and Almaz E 2004 Internal bremsstrahlung spectra of β -particle emitters using the Monte Carlo method *Radiat. Phys. Chem.* **70** 661–8
- de Dreuille O, Strijckmans V, Ameida P, Loc'h C and Bendriem B 1997 Bone equivalent liquid solution to assess accuracy of transmission measurements in SPECT and PET *IEEE Trans. Nucl. Sci.* **44** 1186–90
- Dewaraja Y K, Chun S Y, Srinivasa R N, Kaza R K, Cuneo K C, Majdalany B S, Novelli P M, Ljungberg M and Fessler J A 2017 Improved quantitative 90Y bremsstrahlung SPECT/CT reconstruction with Monte Carlo scatter modeling *Med. Phys.* **44** 6364–76
- Dewaraja Y, Novelli P, Fessler J, Feng M, Nelson R, Rothley J, Ljungberg M, Roberson P and Wilderman S 2015 Y-90 imaging for dosimetry in radioembolization: comparison between scatter corrected bremsstrahlung SPECT/CT and time-of-flight PET/CT *Eur. J. Nucl. Med. Mol. Imaging* **42** (Suppl. 1) S156
- Elschot M, Vermolen B J, Lam M G, de Keizer B, van den Bosch M A and de Jong H W 2013 Quantitative comparison of PET and bremsstrahlung SPECT for imaging the *in vivo* yttrium-90 microsphere distribution after liver radioembolization *PLoS One* **8** e55742
- Fabbi C, Mattone V, Casi M, De F L, Agostini M, Bartolini N, D'ariento M, Marchi G, Bartolomei M and Sarti G 2012 Quantitative evaluation on [90Y] DOTATOC PET and SPECT imaging by phantom acquisitions and clinical applications in locoregional and systemic treatments *Q. J. Nucl. Med. Mol. Imaging* **56** 522–8
- Koral K F, Yendiki A and Dewaraja Y K 2007 Recovery of total I-131 activity within focal volumes using SPECT and 3D OSEM *Phys. Med. Biol.* **52** 777
- Minarik D, Gleisner K S and Ljungberg M 2008 Evaluation of quantitative 90Y SPECT based on experimental phantom studies *Phys. Med. Biol.* **53** 5689
- Minarik D, Sjögreen-Gleisner K, Linden O, Wingårdh K, Tennvall J, Strand S E and Ljungberg M 2010 90Y Bremsstrahlung imaging for absorbed-dose assessment in high-dose radioimmunotherapy *J. Nucl. Med.* **51** 1974–8
- Mougeot X 2015 Reliability of usual assumptions in the calculation of β and ν spectra *Phys. Rev. C* **91** 055504
- Park M, Mahmood A, Zimmerman R E, Limpam-Amara N, Makrigrigorgos G M and Moore S C 2008 Adsorption of metallic radionuclides on plastic phantom walls *Med. Phys.* **35** 1606–10

- Rong X, Du Y, Ljungberg M, Rault E, Vandenberghe S and Frey E C 2012 Development and evaluation of an improved quantitative ^{90}Y bremsstrahlung SPECT method *Med. Phys.* **39** 2346–58
- Salvat F, Fernández-Varea J M and Sempau J 2006 PENELOPE-2006: a code system for Monte Carlo simulation of electron and photon transport *Workshop Proc.*
- Segars W, Sturgeon G, Mendonca S, Grimes J and Tsui B M 2010 4D XCAT phantom for multimodality imaging research *Med. Phys.* **37** 4902–15
- Seltzer S M and Berger M J 1986 Bremsstrahlung energy spectra from electrons with kinetic energy 1 keV–10 GeV incident on screened nuclei and orbital electrons of neutral atoms with $z = 1–100$ *At. Data Nucl. Data Tables* **35** 345–418
- Smits M L, Elschot M, Sze D Y, Kao Y H, Nijsen J F, Iagaru A H, de Jong H W, van den Bosch M A and Lam M G 2015 Radioembolization dosimetry: the road ahead *Cardiovascular Interventional Radiol.* **38** 261–9
- Van Elmbt L, Vandenberghe S, Walrand S, Pauwels S and Jamar F 2011 Comparison of yttrium-90 quantitative imaging by TOF and non-TOF PET in a phantom of liver selective internal radiotherapy *Phys. Med. Biol.* **56** 6759
- Venkataramaiah P, Sanjeeviah H and Sanjeevaiah B 1980 Study of inner bremsstrahlung accompanying beta decay in ^{185}W and ^{90}Y *J. Phys. G: Nucl. Phys.* **6** 1443
- Walrand S, Hesse M, Jamar F and Lhommel R 2018 On the origin and on the reduction of spurious extrahepatic counts observed in ^{90}Y non-tof pet imaging post radioembolization *Phys. Med. Biol.* **63** 075016